Post-Superplastic Forming Analysis Under Different Loading Paths. Part One: Uniaxial Loading Case

F.K. Abu-Farha and M.K. Khraisheh

(Submitted September 19, 2007)

In a previous work, an optimization approach for superplastic forming based on a multiscale stability criterion, and yielding a variable strain rate loading path instead of the commonly used constant strain rate one, was presented. The approach was experimentally validated using the AZ31 magnesium alloy, where it was proven effective in reducing forming time without sacrificing the uniformity of deformation. In this work, the validation process is taken to a different level, where the post-superplastic forming mechanical properties, often ignored in superplasticity, become the criteria. The material is first superplastically deformed under uniaxial loading at an elevated temperature, following both loading paths; constant strain rate versus optimized variable strain rate. Thereafter, specimens extracted from the deformed material are tested at room temperature to evaluate the changes in mechanical properties, in reference to those of the as-received material. The results emphasize on the necessity of a combined forming and post-forming analysis in optimizing the superplastic forming process.

1. Introduction

Superplasticity and the superplastic forming technique are becoming more familiar terms in both the academic research arena and the metal forming industry; a fact embodied by the mounting number of studies in the field, and the increasing number of parts formed using the technique. Furthermore, the escalating demand for lightweight alloys, along with conventional forming techniques' limited capabilities to successfully form such alloys (Aluminum, Titanium, and Magnesium), increases the chances for superplastic forming to secure a good position among advanced future forming techniques. Yet, just like other currently utilized sheet metal forming processes, most of the activities in the field of superplasticity are focused on the material/process level, with very scarce attention paid to the process on the post-forming level (i.e., post-superplastic forming properties). The importance of this specific issue in superplasticity is inherited by the very nature of the process itself, which makes it even a necessity.

Superplastic studies generally target achieving maximum plastic strain, which is very often set as the mere basis for selecting optimum forming parameters, mainly strain rate and temperature. Similarly, higher strain limits and better deformation-uniformity are often the criteria for evaluating the various proposed optimization practices. Such approach could be very misleading, since the conditions for optimum superplasticity in terms of maximum ductility may not necessarily result in optimum values for the mechanical properties, such as tensile strength, ductility, hardness, creep, or fatigue resistance in a formed component. Exposure to elevated temperatures for prolonged periods of time ($>0.5T_m$), very large plastic strains ($>200\%$), and the corresponding microstructural changes (grain growth and severe cavitation), are the factors that might deteriorate the mechanical properties of superplastically formed materials, and therefore need to be studied and quantified in details.

The fact that maximum ductility is often associated with the low strain rate part of the superplastic region has been the main motivation for many investigators to follow a variable strain rate approach, instead of the conventional constant strain rate ones (Ref 1-3). The overall concept of this approach translates into constructing a forming path that starts at a high strain rate value; and as deformation progresses and stability is hindered, strain rate is gradually dropped, maintaining deformation uniformity and therefore preserving the part's integrity. Nevertheless, the selection of such a variable strain rate forming path is not arbitrary, but rather based on the behavior of the material for optimum results. Recently, a new multiscale stability criterion, that takes both geometrical and microstructural features into account, has been developed (Ref 4). The criterion was combined with a simplified uniaxial constitutive model, to optimize the superplastic deformation, and generate the optimum variable strain rate forming path for the AZ31 magnesium alloy at 400 °C (Ref 5, 6).

In this work, the above-mentioned optimum loading path is validated experimentally, to assess its effectiveness in comparison with conventional constant strain rate loading practices. Yet, the validation process is carried out through a combined forming/post-forming approach, where the outcome of the superplastic forming process following each loading path, in terms of the level of deformation-uniformity and the room

F.K. Abu-Farha and **M.K. Khraisheh**, Center for Manufacturing and Mechanical Engineering Department, University of Kentucky, Lexington, KY 40506. Contact e-mail: Khraisheh@engr.uky.edu.

temperature mechanical properties, are evaluated. The focus is directed here to the uniaxial loading case; expanding the investigation to the biaxial loading case is currently being undertaken.

2. General Approach

The general approach for studying the post-superplastic forming properties is simply derived by simulating the response of the material during and after it has been formed into a certain part, and it is best described by the schematic flow chart shown in Fig. 1. It represents an expansion to the efforts of many investigators, like McDarmid (Ref 7), Cope et al. (Ref 8), and Duffy et al. (Ref 9). This systematic approach is not confined to a specific loading case, as demonstrated in previously published general post-SPF investigations (Ref 10, 11). The basic steps presented in the figure are self-explanatory; the remaining details including the selected forming conditions and testing parameters, in addition to the results of this investigation, are all covered in the subsequent sections.

3. Material and Experimental Setup

A 3.22 mm thick AZ31B-H24 commercial magnesium alloy sheets, with an average grain size of 4.5 μm, were used to produce the required test specimens. A 38.1×15.88 mm $(1.5 \times 0.625$ in.) gage section specimens were machined along the rolling direction of the as-received sheets. Though not generally adopted, the quite large section was selected to facilitate producing specimens for the tensile tests needed for the post-SPF analysis part, presented later in Section 6. Specially designed grips for elevated temperature tensile testing were used instead of the conventional sliding-wedge type; the
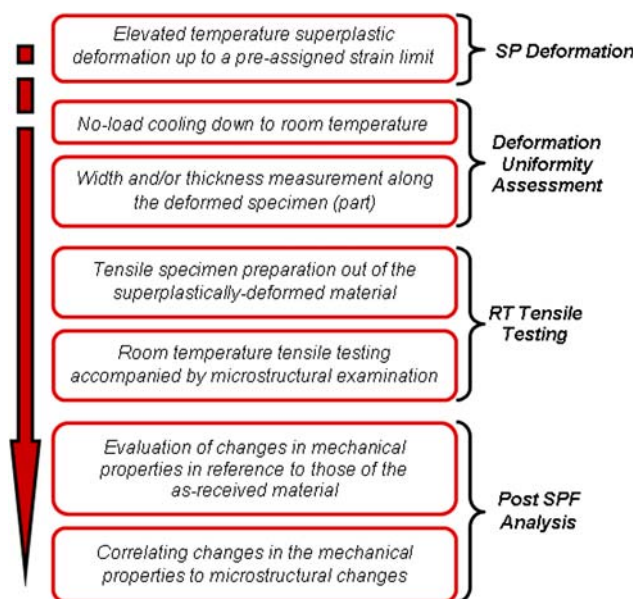
grips and the test specimen's geometry are both shown in Fig. 2.

A 5582 INSTRON load frame, equipped with an electrical resistance heating chamber (furnace), capable of delivering a maximum testing temperature of 610 °C, were used in this work. As will be further elaborated, the setup was first used to impose the uniaxial superplastic deformation in the material (Section 4), and thereafter to evaluate its post-SPF mechanical properties (Section 6). Therefore, two load cells were used accordingly for load monitoring and/or measurement; a 5 kN load cell was used in the superplastic deformation stage, and was replaced by a 100 kN one for the room temperature tensile testing in the post-SPF stage. Analogously, strain measurements were based on the direct displacement of the crosshead beam for the superplastic deformation stage (due to the high temperature and large plastic strains involved), while a 50 mm extensometer was used to ensure accuracy in the post-SPF tensile tests.

4. Uniaxial Superplastic Deformation

Formerly, an integrated optimization approach was proposed by combining a calibrated constitutive model with a modified multi-scale stability criterion, which takes both geometrical and microstructural features into account, and then feeding them into a FE code to generate the desired variable strain rate loading (forming) path. In spite of its significance, the
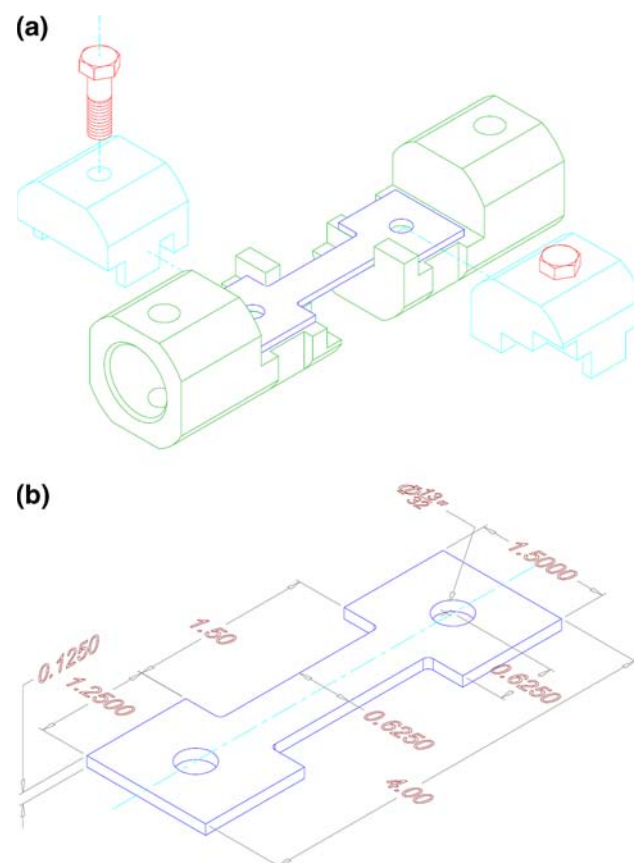

Fig. 1 Schematic approach to investigating the post-superplastic forming properties

Fig. 2 (a) Grips for high temperature tensile testing and (b) Test specimen's geometry

aforementioned analysis is out of the scope of this work, and will not be presented or discussed here; detailed description of the constitutive model, the stability criterion, and the proposed optimization scheme can be found in previous publications (Ref 4, 5, 11, 12). For the AZ31 magnesium alloy, at 400 °C in particular, the generated optimum forming path has the form given in Fig. 3(a).

The load frame cannot impose such a variable strain rate loading path; therefore, the curve in Fig. 3(a) had to be converted into a variable speed loading path. To do so, the curve was first approximated by multisteps of constant strain rates, and then each was converted into several steps of constant speed, such that the error in strain rate did not exceed ±2.5%. As a result, the final optimum variable speed loading path is shown in Fig. 3b, and it is composed of about 40 constant speed segments. Naturally, this approximation process could be further refined by increasing the number of constant strain rate steps, and dropping the maximum error limit.

Uniaxial superplastic deformation was imposed on a number of tensile test specimens at 400 °C by following the optimum loading path in Fig. 3(b). Heating to the forming temperature took about 35 min, followed by 30 min dwell time to achieve thermal equilibrium. The different specimens were stretched to selected true strain values of 0.5, 0.7, 0.9, 1.1, and 1.3; thereat each test was stopped, and the corresponding specimen was cooled down to room temperature in 60 min while maintaining no load. Each one of the five strain limits was covered by at least three specimens to ensure repeatability.

Since the actual strain rate is changing from a high to a low value throughout each one of these tests, the stress/strain curve is expected to resemble such a change. Figure 4 shows how the overall stress/strain curve of the optimum loading path compares to those corresponding to a band of constant strain rates. As expected, instead of a smooth curve, each drop in speed (or equally strain rate) in Fig. 3(b) results in an abrupt drop in flow stress in Fig. 4, and vice versa. Yet, it is more interesting to observe that the optimized stress/strain curve is, more or less, confined within a region bounded by a line connecting the peak points of all the other stress/strain curves. This in fact embodies the very nature of the optimum forming path of the material in Fig. 3(a), where the limiting stable strain at each strain rate is roughly the strain corresponding to the peak point of each curve.

Additional tensile test specimens were superplastically stretched to the same strain values at two constant strain rates for comparison. 1×10^{-3} s^{-1} was selected as a fast forming rate, and 1×10^{-4} s^{-1} as a slow forming rate.

5. Superplastic Deformation Uniformity

In order to evaluate deformation uniformity, width and thickness distributions, along the gage section of each specimen, were measured and recorded for every combination of strain rate and strain limit. The "evolution" in terms of both width and thickness can be traced as deformation progresses at any strain rate. By normalizing with respect to the initial dimensions, percentage drop of width and thickness are plotted along the gage length for the deformed specimens in Fig. 5. Parts (b) and (c) of the figure generally show how significant the drop in both thickness and width become, in addition to their variation along the specimen, as deformation progresses. Expectedly, regardless of the true strain limit, 1×10^{-4} s^{-1} always yields the best deformation uniformity, in terms of both width and thickness. Yet, a closer look at the curves corresponding to the optimum loading path, in comparison with the high and low strain rate ones, reveals few interesting observations.
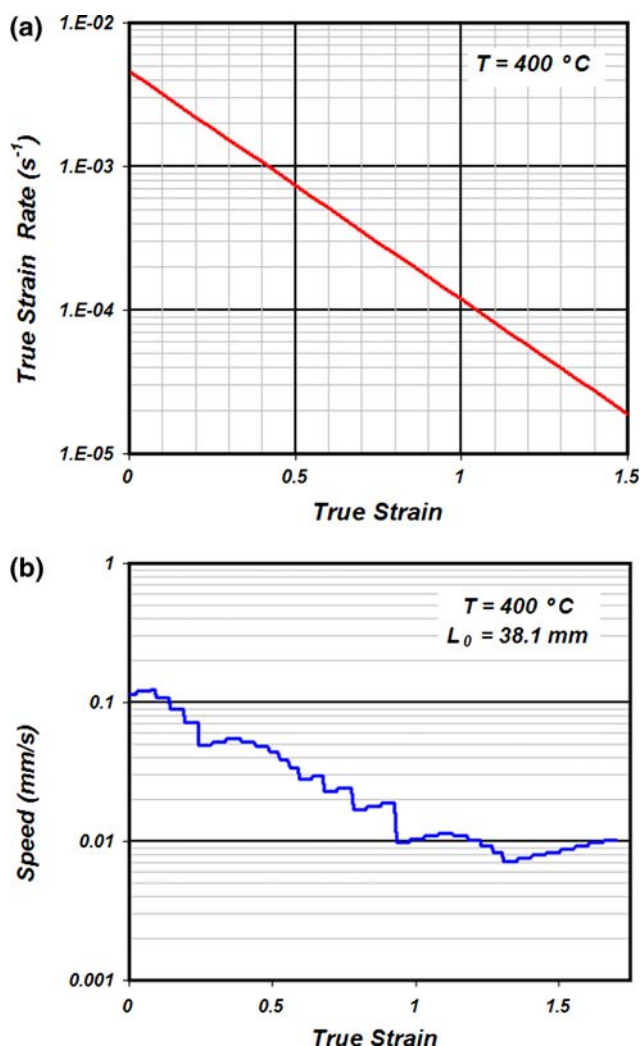
Fig. 3 Optimum forming path for the AZ31 magnesium alloy at 400 °C in terms of (a) Strain rate and (b) Speed
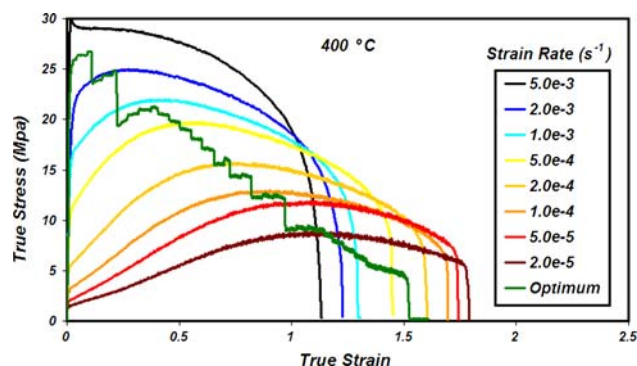
Fig. 4 Stress/strain curve based on the optimum loading path compared to those corresponding to constant strain rates
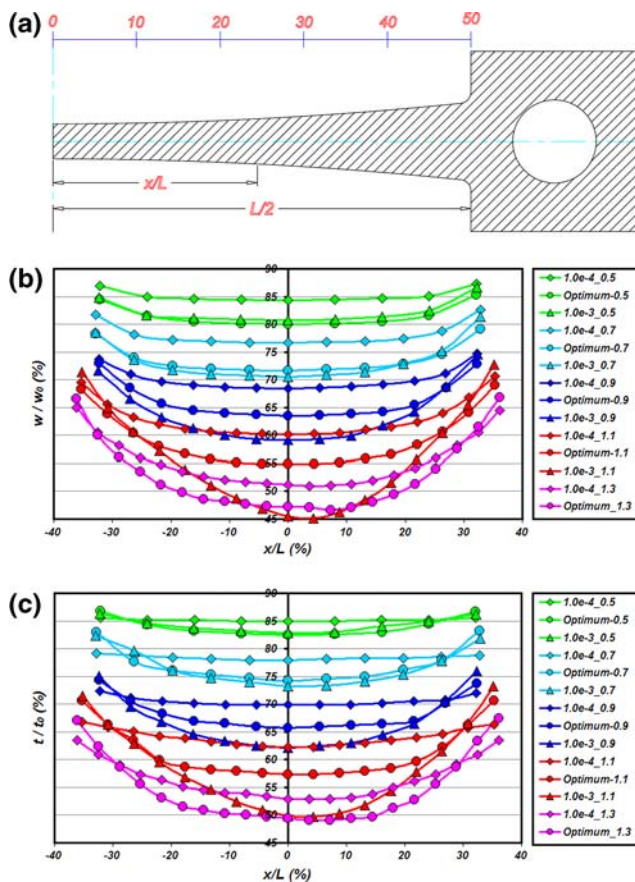
Fig. 5 (a) Schematic of a deformed specimen; (b) Normalized width distributions along specimens strained to various strains; and (c) Normalized thickness distributions along specimens strained to various strains

For the specimens stretched to 0.5 true strain, the worst deformation uniformity is observed in the case of the optimum loading path, and not fast forming at 1×10^{-3} s^{-1}. By referring to Fig. 3(a), one can observe that the segment of the optimum curve stretching to 0.5 true strain, lies almost entirely above the 1×10^{-3} s^{-1} line, which implies faster forming to that strain limit. This should not be taken as a drawback of the optimized approach, since the difference in deformation uniformity between the optimum and the 1×10^{-3} s^{-1} cases is very small, and does not add to the more substantial difference already existing between the 1×10^{-3} and 1×10^{-4} s^{-1} cases. On the other hand, time saving by optimization, in comparison to slow forming at 1×10^{-4} s^{-1}, is quite considerable (about 12 folds), as inferred from the summary of forming times and thinning given in Table 1. This, in fact, represents the essence of the optimization approach, by achieving as much time-savings as possible; and forming to quite small strain limits is the ideal situation to do that, without sacrificing deformation uniformity.

As superplastic deformation progresses, optimum loading yields deformation uniformity in between the two extremes of either slow or fast forming, in some sort of a balance that sustains maximum forming time savings. Such balance could be best observed by noticing how the width and thickness distribution curves resulting from the optimum loading path are initially closer to those corresponding to the 1×10^{-3} s^{-1} rate for strain limits below 0.9, but become closer to those

corresponding to the 1×10^{-4} s^{-1} rate for strain limits above 0.9. The same analogy applies by following the changes in forming time corresponding to the optimum loading path with respect to the other two constant strain rates, all listed in Table 1.

Overall, and in reference to the ideal case of forming at the low strain rate of 1×10^{-4} s^{-1}, optimized forming yields a seemingly fixed drop in deformation uniformity, while the drop caused by fast forming at 1×10^{-3} s^{-1} keeps diverging as deformation progresses. The divergence escalates after 1.1, and the specimens formed at 1×10^{-3} s^{-1} finally fail at about 1.19 true strain (about 230% tensile strain). The optimized specimens, on the other hand, maintain descent deformation uniformity combined with significant forming time savings, until failure at about 1.58 true strain (about 385% tensile strain), which is considered quite large. To finalize the comparison, it is worth mentioning that the specimens strained at 1×10^{-4} s^{-1} failed at about 1.7 true strain (about 445% tensile strain).

Finally, the former discussion regarding the results presented in Fig. 5 is further elaborated by Fig. 6, which shows samples of the specimens superplastically strained to various levels, following the three different loading paths. The effectiveness of the proposed optimization scheme is clearly emphasized; not only forming time is significantly reduced without compromising deformation uniformity, but also uniform deformation is maintained until the thresholds of failure. The importance of this conclusion is derived from actual forming practices, in which deformation uniformity is as important as ductility limits. In other words, achieving high ductility is virtually impractical, unless it is coupled with good deformation uniformity.

Out of each curve corresponding to a certain combination of strain and strain rate in Fig. 5, the point of maximum percentage drop is extracted, and the somewhat cumbersome normalized width and thickness distribution curves are replaced by the two graphs shown in Fig. 7. These plots summarize the mutual influence of the two forming parameters, strain limit and strain rate (whether fixed or variable), on the uniformity of uniaxial superplastic deformation achieved at 400 °C. It is clear that the critical points highlighted in the above-mentioned discussion are well resembled in these few curves. To draw the attention here, notice the nearly-parallel relationship between the optimum thinning curves and the ones corresponding to 1×10^{-4} s^{-1}, in comparison to those corresponding to 1×10^{-3} s^{-1}, which diverge away as superplastic deformation progresses.

It should be emphasized, at this point, that plots such as the ones presented so far do not imply nor encourage forming at lower strain rates for better deformation uniformity results, but rather provide the background for choosing the fastest "satisfactory" loading path to achieve the desired uniformity level for a particular strain limit, which is embodied in this case by the proposed optimization scheme.

The curves shown in Fig. 7 are plotted against the longitudinal strain of the tensile specimens, which is a common practice when presenting any quantity in uniaxial superplastic deformation. Yet by doing so, it is implied that the deformation is uniform all along the specimen; an assumption that has been quite established as inaccurate. Therefore, it is more precise to plot results of such nature against the true effective strain, which takes actual width and thickness strains into account. And since both width and thickness were already measured and recorded, the corresponding strains, and consequently the effective strains, were all evaluated, and plotted along each

Table 1 Forming time vs. thinning for the various combinations of strain limits and loading paths (strain rate)

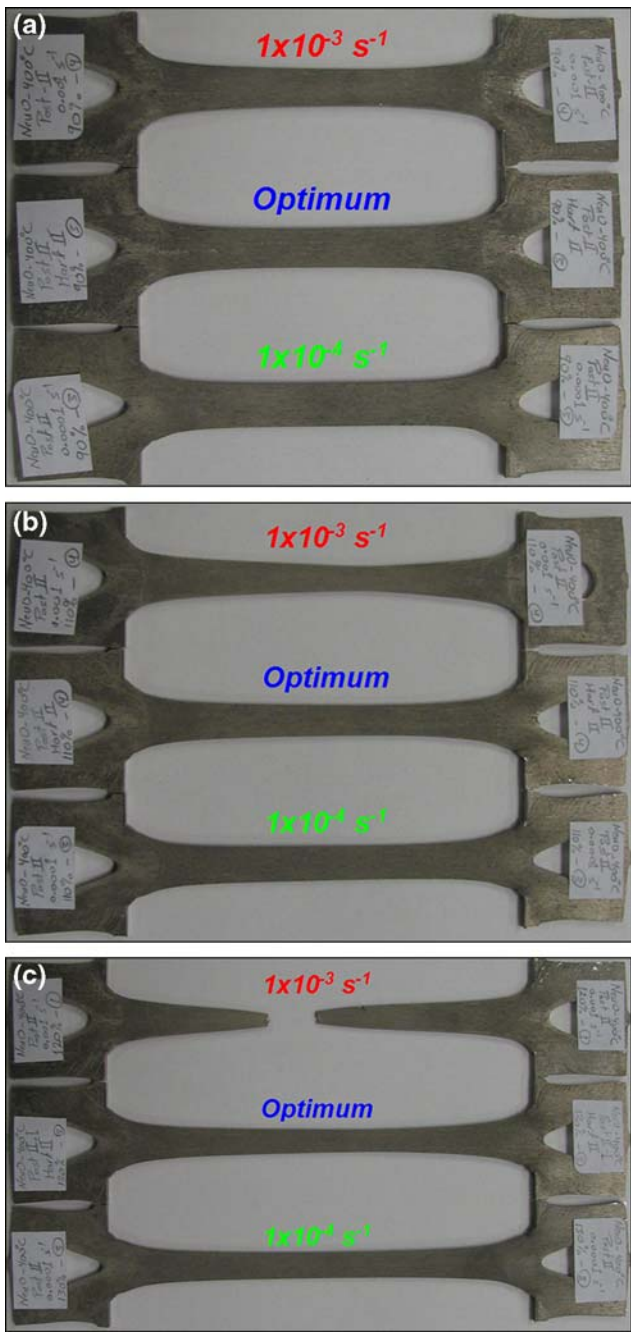| Strain rate, s^{-1} | Forming time [min] | | | | | |
| | Thinning $\{t_{Min}/t_0\}$ | | | | | |
	0.5	0.7	0.9	1.1	1.3	Failure
1×10^{-3}	[8.33]	[11.67]	[15]	[18.33]	Failed at	...
	{0.828}	{0.731}	{0.615}	{0.493}	1.19	...
1×10^{-4}	[83.33]	[116.67]	[150]	[183.33]	[216.67]	Failed at
	{0.851}	{0.780}	{0.699}	{0.623}	{0.528}	1.70
Optimum	[6.53]	[14.01]	[28.50]	[61.05]	[102.08]	Failed at
	{0.825}	{0.742}	{0.657}	{0.571}	{0.491}	1.58

Fig. 6 Specimens superplastically deformed at different loading paths to (a) 0.9; (b) 1.1; and (c) 1.3 true strain limits
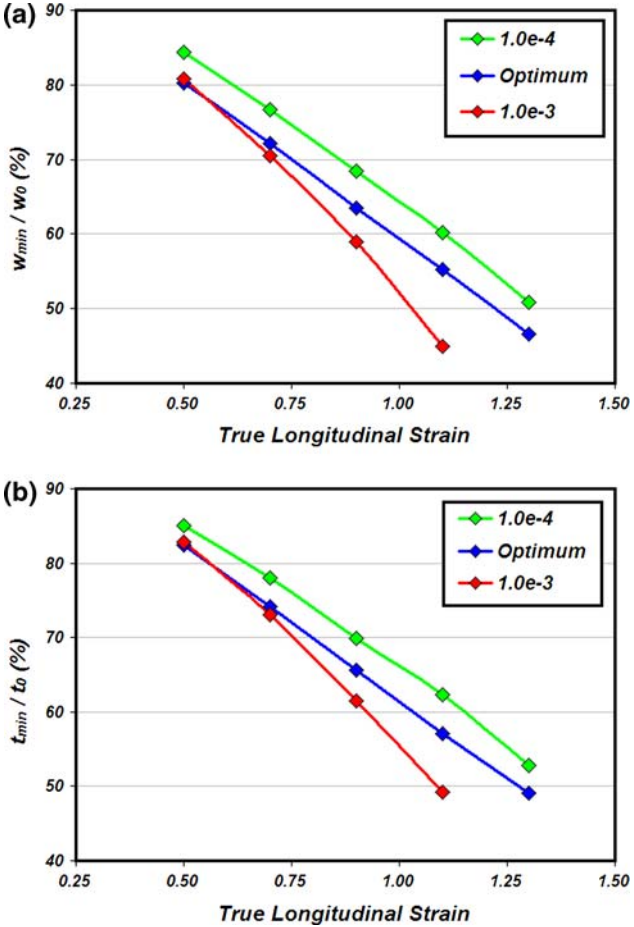

Fig. 7 Maximum thinning versus true longitudinal strain in terms of (a) Width and (b) Thickness

specimen. An example is shown in Fig. 8; where width, thickness and effective strains are plotted along a specimen deformed according to the optimum loading path to 1.3 true longitudinal strain. Ideally, longitudinal and effective strains are equal under uniaxial loading conditions; yet Fig. 8 shows that the effective strain varies between −40 and +14% of the longitudinal one, for this particular case. Such variation quantitatively describes how localized the deformation is, and how misleading it would be to assume uniform longitudinal strain all along the specimen.

By focusing on the point of maximum thinning in each specimen, the two parts of Fig. 7 were re-plotted against the
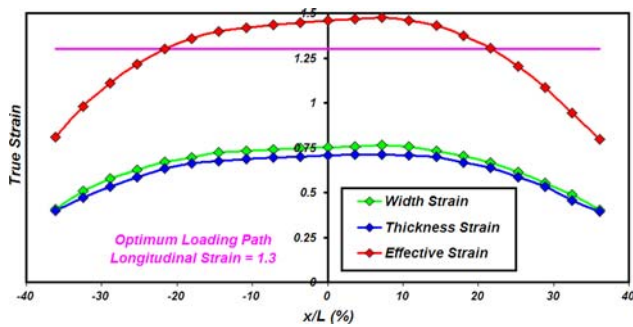
Fig. 8 Width, thickness, and effective strain along a specimen deformed to 1.3 true longitudinal strain according to the optimum loading path
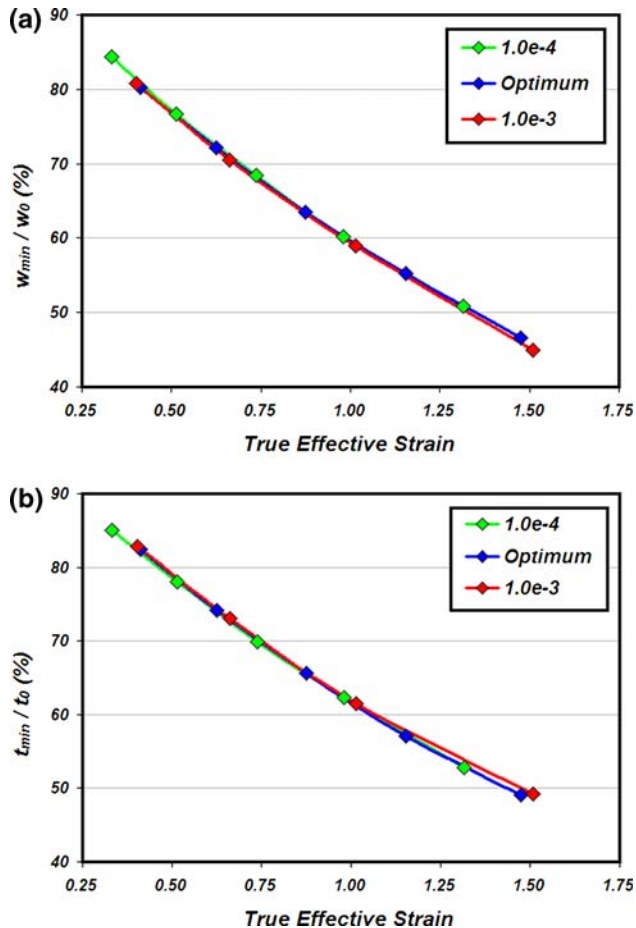

Fig. 9 Maximum thinning versus true effective strain in terms of (a) Width and (b) Thickness

Fig. 10 (a) Width strain versus true longitudinal strain and (b) Thickness strain versus true longitudinal strain

effective strain at that point, and the results are shown in Fig. 9. The curves in each one of the new plots greatly match, suggesting that loading path (constant or variable, fast or slow) has no effect on the trend by which deformation uniformity (quantified in terms of maximum thinning) varies with respect to effective strain.

To explain the seemingly contradiction with Fig. 7, maximum width and thickness strains were plotted against longitudinal strain for the three loading paths, as shown in Fig. 10. The plots show that the higher the forming rate is, the larger
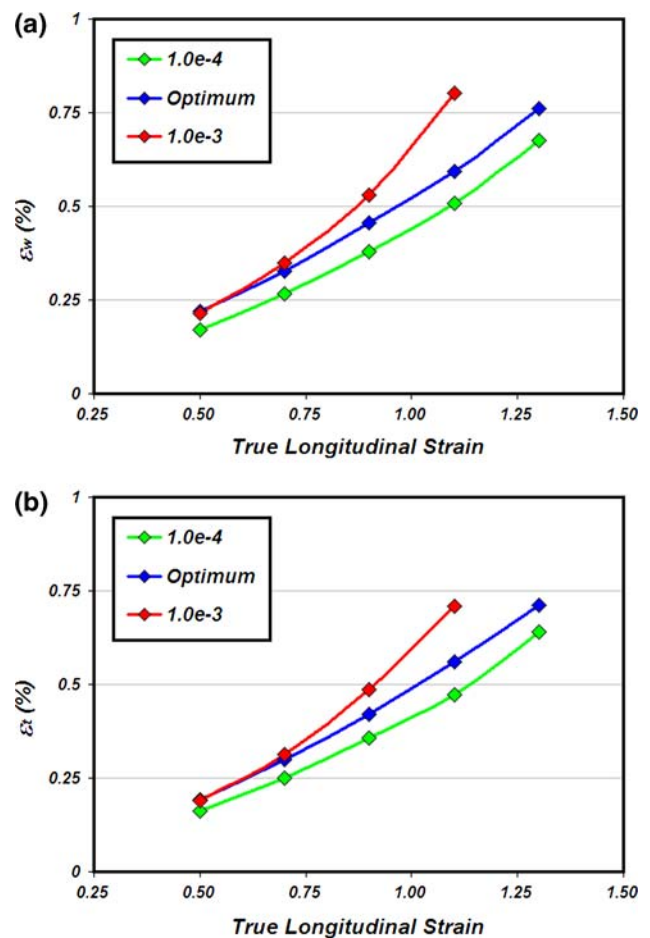
the resulting strains are, for the same longitudinal strain. Practically, this would be mirrored by the fact that higher strain rate forming leads to more localized deformation, as depicted from both Fig. 5 and 6. So by re-plotting the curves in Fig. 7 with respect to the effective strain instead, each point shifts horizontally by a distance proportional to the degree of deformation localization, causing greater shift at higher strain rates, and ultimately aligning the various curves along the same path. Similar behavior is noticed when re-plotting the width and thickness strain curves of Fig. 10 with respect to the effective strain, as shown in Fig. 11.

In summary, even though the two presentations seem to lead to different conclusions, plotting the results against longitudinal or effective strains should be equivalent, provided that enough attention is paid when reading the results. The strong influence of loading path on deformation uniformity is straightforwardly sensed when considering longitudinal strain, simply because it is (i.e., the longitudinal strain) considered independent of the loading path anyway. Therefore, when reading analogous results plotted against the effective strain, one should bear in mind that effective strain itself is highly dependent on the loading path in the first place. It is vitally important to be aware of this in actual superplastic forming practices, where more complicated multiaxial loading conditions are involved, and effective strain is the only mean to describe results of such nature.
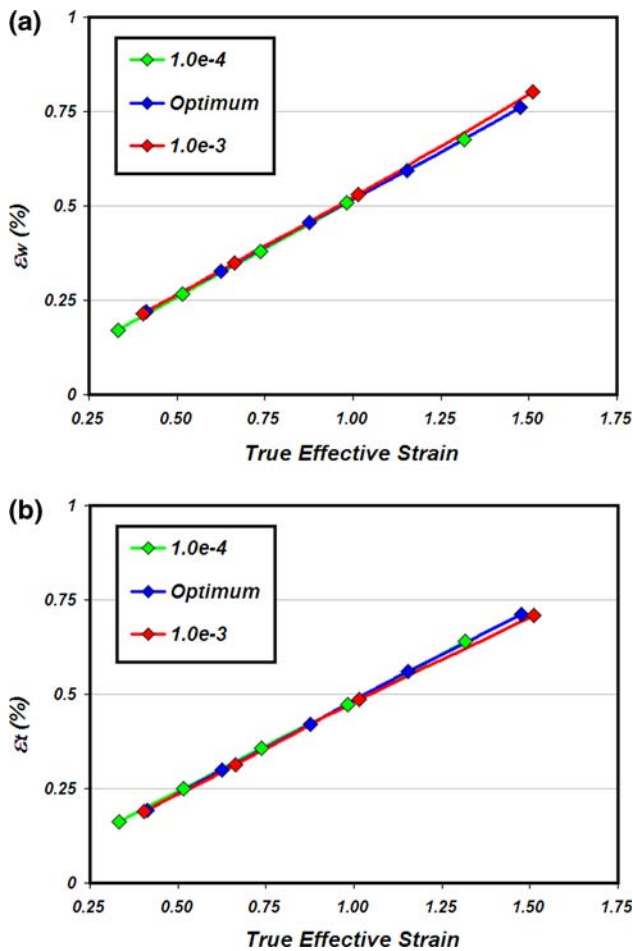
Fig. 11 (a) Width strain versus true effective strain and (b) Thickness strain versus true effective strain

Fig. 12 Normalized post-SPF yield strength versus true (a) Longitudinal strain and (b) Effective strain

6. Room Temperature Tensile Testing and Post-Superplastic Forming Mechanical Properties

Following deformation uniformity assessment, all the specimens were machined along the sides to produce a uniform section. Despite the various lengths of the specimens deformed to different strain limits, only 60 mm of the gage section was machined, in order to further localize deformation in the subsequent room temperature tensile testing. A 60 mm extensometer was not chosen randomly, but rather deliberately to guarantee enough room for a 50 mm extensometer, which was used for more accurate strain measurements. Thickness, on the other hand, was not altered to avoid distorting the specimens; besides, thickness variation was minimal around the center of the deformed specimens within a 50 mm circle. The machined specimens were then tested in simple tension at room temperature, at a constant speed of 1.5 mm/min to evaluate the post-SPF mechanical properties.

For each specimen superplastically deformed at a certain combination of strain and strain rate, three main quantities were extracted from the subsequent room temperature tensile test: yield strength, ultimate tensile strength, and fracture strain. Yet, the absolute values of mechanical properties are not of prime interest, since the ultimate goal of this analysis is to arrive at a quantitative
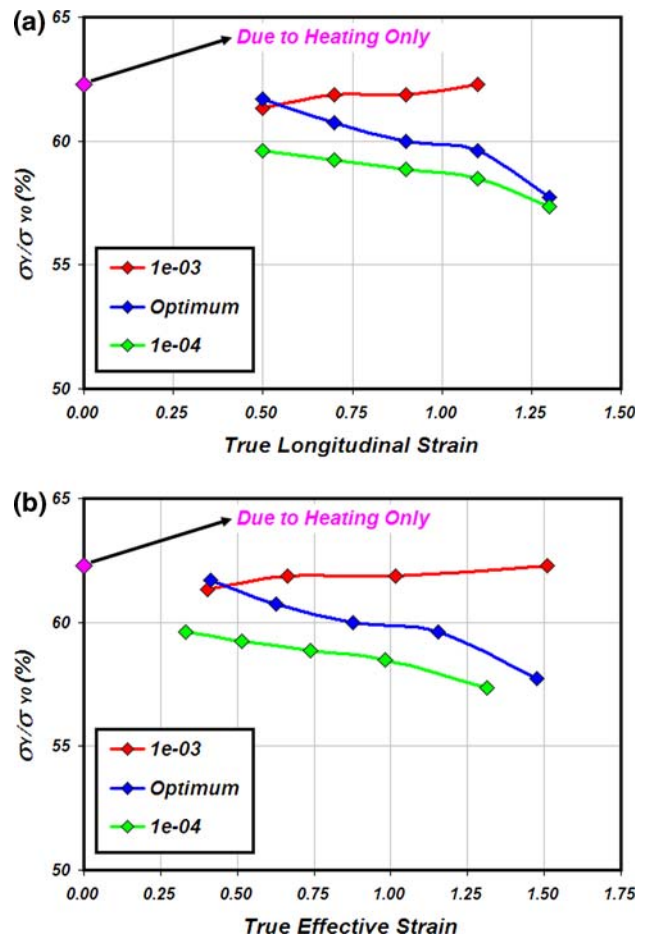
assessment of the "changes" in the yield strength, ultimate tensile strength, and room temperature ductility caused by superplastic deformation at various strains and strain rates. Therefore, these quantities were normalized by comparing them to the corresponding mechanical properties of the as-received material, obtained by similar tensile tests on un-deformed specimens. The results are summarized in the following few figures.

Post-SPF yield strength results were different from both ductility and ultimate tensile strength, in regard to their insensitivity to strain and strain rate. Figure 12(a) indicates that neither parameter shows any significant impact, where yield strength of the post-SPF material varies between 58% and 62% of that corresponding to the as-received material. Apart from that, the figure accentuates on the clear impact of superplastic forming on deteriorating the material's yield strength, embodied by the large overall drop of around 40%. And since neither strain nor strain rate seem to be responsible for this, heat must be the cause. To investigate that, a simplified heating cycle analysis was carried out, in which tensile specimens were heated to 400 °C and then cooled down to the ambient temperature without straining. Room temperature tensile testing was similarly carried out on those specimens, and revealed about 38% drop in yield strength with respect to the as-received material, as highlighted in the figure.

It is believed that this huge drop in yield strength is primarily associated with the microstructural changes in the

material caused by heating (Ref 10). In previous works, a complete grain growth analysis during superplastic forming of the studied alloy at 400 °C, covering both the static and dynamic parts, was carried out (Ref 11). The analysis revealed strong static growth with a high rate of change during the heating phase, which slowly dampens with the subsequent dynamic growth as deformation progresses. Results showed that static grain growth takes place predominantly within the first 65 min of heating time, where grains grow from 4.5 to about 8 μm. And since this amount of time is equal to the total heating time prior to straining (as was described earlier in Section 4), then the initial grain size at the threshold of superplastic deformation is actually 8 μm, and not 4.5 μm. This explains why the thermally cycled specimens exhibited 38% drop in yield strength; such behavior is consistent with the well-known Hall-Petch relationship.

In summary, it is concluded that post-SPF yield strength is solely affected by heating (in terms of both temperature and time); the curves in Fig. 12(a) demonstrate how infinitesimal the effect of straining is on the post-SPF yield strength, compared to that of heating. Re-plotting the same curves against effective strain instead, as shown in Fig. 12(b), does not alter the conclusion in this regard.

Post-SPF tensile strength results, on the other hand, are first plotted against longitudinal strain in Fig. 13(a), where the dependency on both strain and loading path is noticed. In terms of strain, the curves show an overall steady decline up to about
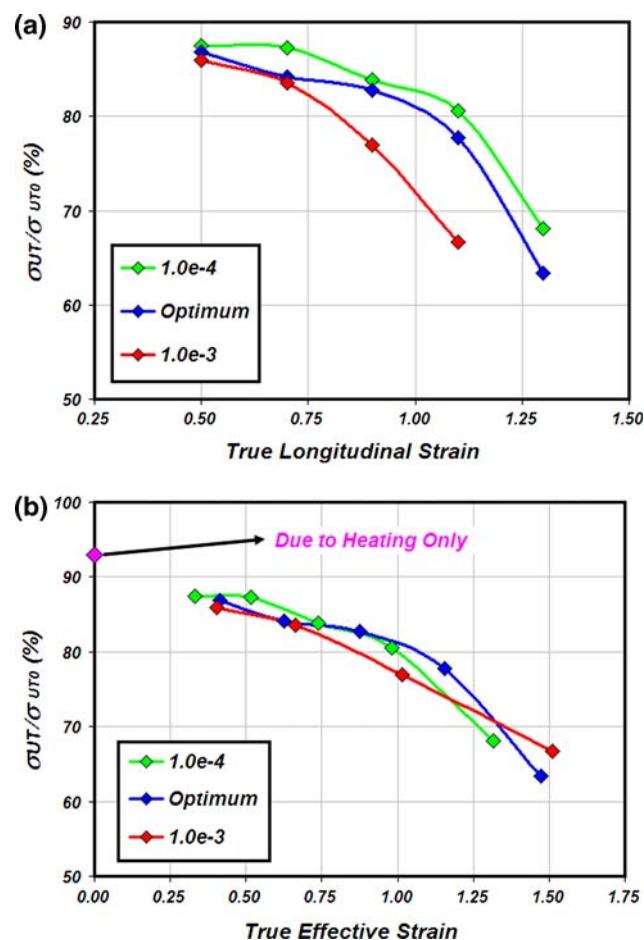
1.1 true superplastic strain, beyond which tensile strength shows a more drastic drop. And in terms of loading path, the influence is sensed by the divergence between the outcomes of the fastest and slowest strain rates. Notice that the optimum loading path yields an intermediate outcome all along, as it deviates from the fast-declining high strain rate, and gets closer to the low strain rate as deformation progresses.

By extrapolating to very small strains, the material seems to have lost about 10% of its tensile strength, which cannot have been caused by strain. Heating cycle analysis showed that nonsuperplastically deformed specimens exhibited about 7% drop in their tensile strength due to heating only. Just like yield strength, ultimate tensile strength is inversely proportional to the initial grain size, according to the Hall-Petch relationship, even if not to the same extent. On the other hand, it is believed that the subsequent decline in post-SPF tensile strength is mainly driven by cavitation, which was previously investigated, and was shown to escalate exponentially with superplastic strain (Ref 6).

Though the three curves in Fig. 13(a) follow a trend that seems to be mainly driven by strain, loading path shows stronger influence at higher strain limits, where more drop in tensile strength is noticed at higher strain rates. Nevertheless, the influence almost diminishes as the same results are plotted against the true effective strain, as shown in Fig. 13(b). This is quite similar to the general behavior observed and highlighted earlier in the deformation uniformity part; therefore, the same argument regarding effective strain's sensitivity to loading path applies here.
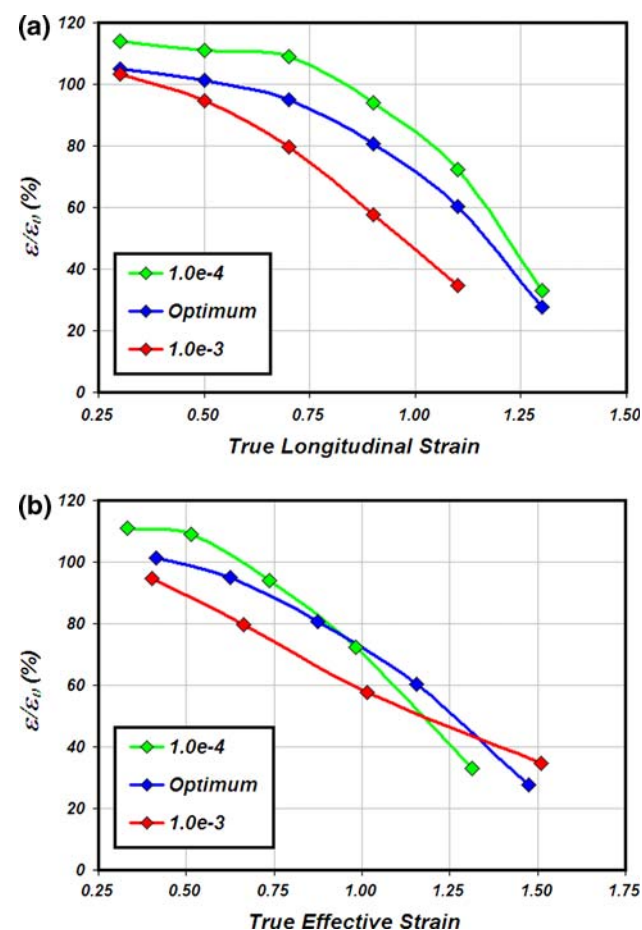

Fig. 13 Normalized post-SPF tensile strength versus true (a) Longitudinal strain and (b) Effective strain

Fig. 14 Normalized post-SPF ductility versus true (a) Longitudinal strain and (b) Effective strain

The last of the three mechanical properties, post-SPF room temperature ductility (fracture strain), is plotted against longitudinal strain in Fig. 14(a), indicating clear influence of both strain and loading path. The trend is somewhat expected; the higher the superplastic strain and strain rate, the lower the post-SPF ductility is. Similar to the previous case of ultimate tensile strength, the adverse effect of these two parameters is initially small, but increases dramatically as superplastic deformation progresses to higher strain limits; again cavitation is believed to be the driving mechanism for such behavior. Yet unlike strength, Fig. 14(a) shows an interesting observation of high fracture strain ratios ($\varepsilon/\varepsilon_0$) that exceed 100%, for all small strains, regardless of the applied followed path. These ratios imply that superplastic deformation, up to a certain limit, causes some ductility enhancement, before it gradually decreases as higher strains are achieved. Heat cycling analysis supported this observation, yielding about 23% increase in room temperature ductility over the as-received materials. Grain growth provides the explanation, since the material gets closer to the O-temper by heating, which is less strain hardened and therefore more ductile (compared to the as-received material AZ31B-H24, which is partially hardened).

Finally, the general impression for loss of sensitivity to loading path, when the results are plotted against effective strain, is noticed again in Fig. 14(b).

7. Post-Superplastic Forming Microhardness

For each of the loading path/strain limit combinations that were covered in the superplastic deformation part, a tensile specimen was selected for investigating the post-SPF microhardness. Each of the selected specimens was cut in half at the maximum thinning point, and two samples were extracted and then molded, such that the top section (top surface of the tensile specimen) is exposed in one, while the cross section is exposed in the other. All the mounted samples were ground and polished according to the ASM standard procedures to produce the appropriate surface finish (just as in preparing magnesium samples for microstructural examination). Ten microhardness measurements were taken per sample, the average of which was denoted as the value (either HV_T or HV_C) for the corresponding superplastic strain in the tensile specimen. The same was carried out for samples of the as-received and heat-cycled materials. All the measurements were normalized with respect to the corresponding as-received material's micro-hardness values, and the results were plotted against longitudinal strain, as shown in both parts of Fig. 15.

The clearest influence of heat, strain and loading path on a post-SPF quantity is observed here. This applies to both top surface (HV_T) and cross section (HV_C) microhardness, although they are noticeably different, with the cross section one being generally higher. Interestingly, the values corresponding to the as-received material (HV_{T0} and HV_{C0}) were estimated to be equal.

The effect of heating is evident from the 20-25% initial drop in microhardness, exhibited by the heat-cycled specimens. This is hardly surprising, provided that heating softens the alloy, and brings it closer to the O-temper condition. For comparison, typical Rockwell hardness values for the AZ31B-O magnesium alloy are roughly 20% lower than those for the AZ31B-H24 one (Ref 13).
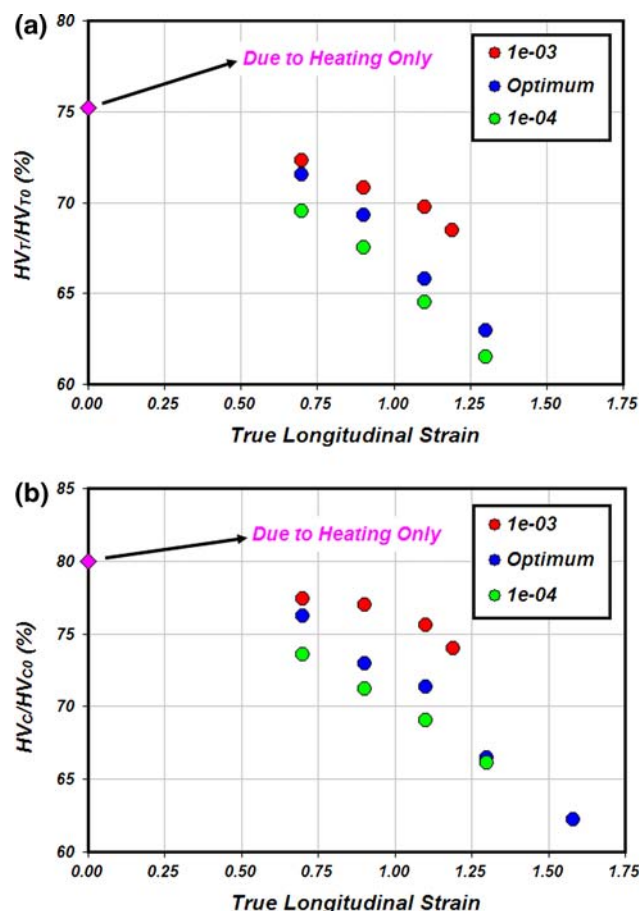

Fig. 15 Normalized post-SPF microhardness versus longitudinal strain, measured on (a) Top surface and (b) Cross section

The subsequent drop in post-SPF micro-hardness seems to be driven by both strain and loading path; however, the behavior is opposite to that in the case of the other mechanical properties, tensile strength, and ductility in particular. The curves demonstrate comparable inverse proportionality to longitudinal strain, yet this proportionality increases as strain rate decreases, on the contrary to Fig. 13 and 14 where it increases with strain rate. It is believed that heating remains an influential factor in the case of microhardness, even while deformation is taking place. Only this time, the combination of strain and loading path determines the amount of exposure time to the elevated temperature, and consequently further escalates the drop in the material's microhardness.

To support this argument, Fig. 16 presents the same post-SPF microhardness data points against true effective strain. Unlike all the previous curves, this is the only quantity that does not follow the trend of seemingly insensitive influence for that loading path, when effective strains are considered. Contrarily, its influence becomes more apparent this way, and the straight lines corresponding to the two constant strain rates in both parts of the figure further illustrate that. When extrapolated, each line stretches back to the same point, which corresponds to the heat-cycled material, and then travels at a slope that is higher for the lower strain rate. On the other hand, the points corresponding to the optimum loading path do not follow the same linear trend, simply because the strain rate keeps changing. Yet, they still reflect the nature of the optimized approach, as they diverge away from the high strain
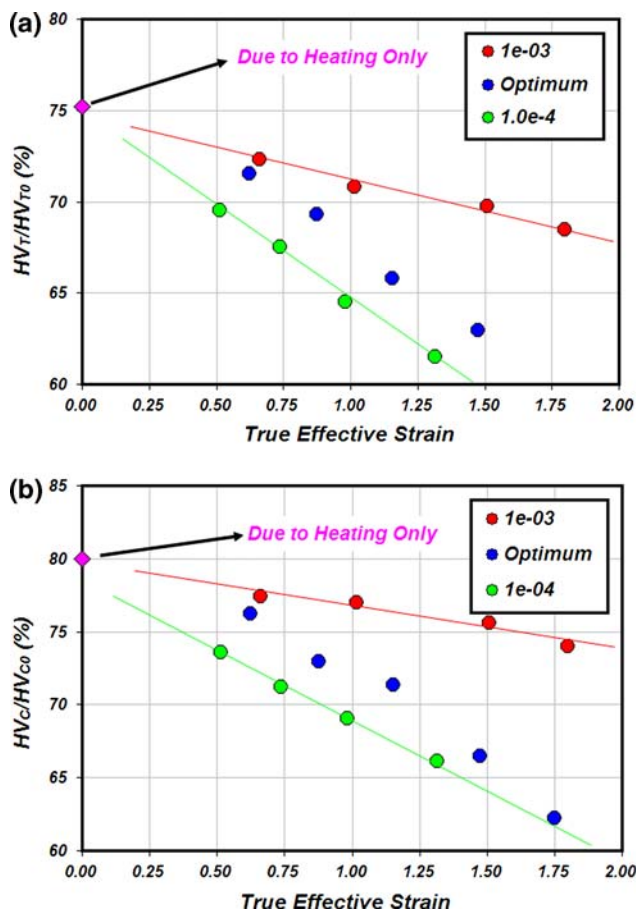
Fig. 16 Normalized post-SPF microhardness versus effective strain, measured on (a) Top surface and (b) Cross section

rate line and approach the low strain rate one, as deformation progresses.

Finally, the overall difference between HV_T and HV_C values is possibly caused by the difference in the grain structure of the material, when observed from the corresponding sections. For instance, the grain growth investigation mentioned earlier and used to explain some of the changes in the post-SPF mechanical properties, was merely based on the cross section of the studied material samples (Ref 11). Further information about dynamic grain growth in both sections (top versus cross section), in terms of shape and rate of size change, might help explain the difference.

8. Remarks

All together, deformation uniformity and mechanical properties (including microhardness) were all shown to be affected, in different ways and to varying levels, by superplastic deformation. The results presented in this work testify to the critical importance of the issue of post-forming analysis, particularly in superplastic forming, and the need to combine it with a forming analysis, for proper selection of process parameters. It is quite clear how misleading it would be to select a certain material for a specific application, based only on its mechanical properties in the as-received condition, without accounting for the changes induced by the superplastic forming process itself.

Particular attention was paid to the impact of following an optimized variable strain rate loading path versus a conventional constant strain rate one, in forming the material superplastically. The pre-developed optimization scheme was experimentally validated, not only in terms of time-savings, but also deformation uniformity and post-forming mechanical properties. The results emphasize on the need for a post-forming analysis for a more proper optimization of the superplastic forming process.

Throughout this work, both deformation uniformity and post-superplastic forming mechanical properties have been deliberately presented in two ways, in order to highlight a general observation: loading path has a noticeable influence on the results when longitudinal strains are considered, yet it seems to diminish when considering effective strains instead. It was explained how both presentations are equivalent, for the uniaxial loading case considered in this effort; yet more attention must be paid to the other multiloading cases embodied by actual superplastic forming practices.

For broader and more comprehensive understanding, this investigation is currently being expanded to the biaxial loading case.

References

1. C. Johnson, C.H. Hamilton, H.M. Zbib, and S. Richter, Designing Optimized Deformation Paths for Superplastic Ti6Al4V, *Advances in Superplasticity and Superplastic Forming*, N. Chandra et al., Ed., Metals and Materials Society, 1993, p. 3–15
2. X.D. Ding, H.M. Zbib, C.H. Hamilton, and A.E. Bayoumi, On the Optimisation of Superplastic Blow-Forming Processes, *J. Mater. Eng. Perform.*, 1995, **4**, p 474–485
3. M.K. Khraisheh and H.M. Zbib, Optimum Forming Loading Paths for Pb-Sn Superplastic Sheet Materials, *J. Eng. Mater. Technol.*, 1999, **121**, p 341–345
4. N. Thuramalla and M. Khraisheh, Multiscale-Based Optimization of Superplastic Forming, *Trans. NAMRI/SME*, 2004, **32**, p 637–643
5. M.A. Nazzal, M.K. Khraisheh, and B.M. Darras, Finite Element Modeling and Optimization of Superplastic Forming Using Variable Strain Rate Approach, *J. Mater. Eng. Perform.*, 2004, **13**, p 691–699
6. M.K. Khraisheh, F.K. Abu-Farha, M.A. Nazzal, and K.J. Weinmann, Combined Mechanics-Materials Based Optimization of Superplastic Forming of Magnesium AZ31 Alloy: Model Development and Experimental Validation, *Ann. CIRP*, 2006, **55**, p 233–236
7. D.S. McDarmid, Superplastic Forming and Post-Forming Tensile Properties of High Strength Titanium Alloy Ti-4Al-4Mo-2Sn-0.5Si, *Mater. Sci. Eng.*, 1985, **70**(1-2), p 123–129
8. M. Cope, D. Evetts, and N. Ridley, Post-Forming Tensile Properties of Superplastic Ti-6Al-4V Alloy, *Mater. Sci. Technol.*, 1987, **3**(6), p 455–461
9. L.B. Duffy, J.B. Hawkyard, and N. Ridley, Post-Forming Tensile Properties of Superplastically Bulge Formed High Strength α/β Ti-Al-Mo-Sn-Si Alloy (IMI 550), *Mater. Sci. Technol.*, 1988, **4**(8), p 707–712
10. M.K. Khraisheh, F.K. Abu-Farha, and K.J. Weinmann, Investigation of Post-Superplastic Forming Properties of AZ31 Magnesium Alloy, *Ann. CIRP*, 2007, **56**(1), p 289–292
11. F.K. Abu-Farha, "Integrated Approach to the Superplastic Forming of Magnesium Alloys," Ph.D. Dissertation, University of Kentucky, 2007
12. M.K. Khraisheh and F.K. Abu-Farha, Microstructure-Based Modeling of Anisotropic Superplastic Deformation, *Trans. NAMRI/SME*, 2003, **31**, p 41–47
13. www.magnesium-elektron.com